Investigation of impact of calcination temperature on the structural, microstructural, and functional properties of MgO nanoparticles using Williamson Hall method

A. Tanveer, M. M. Haseeb Awan, and M. Sajjad Mehmood

Department of Physical Sciences, University of Engineering and Technology, 47050, Taxila, Pakistan.

M. Ahmad

Department of Physics, International Islamic University Islamabad, Pakistan.

Received 3 December 2025; accepted 26 May 2026

Magnesium oxide (MgO) nanoparticles were synthesized using a co-precipitation method and then calcined at 450 °C, 650 °C, and 700 °C to study the effects of different calcination temperatures on the structure and microstructure. The phase composition of the synthesized samples was studied using X-ray diffraction (XRD), which showed that all samples were composed of single-phase cubic MgO, and no secondary phases were detected. The Williamson-Hall (W–H) analysis using Lorentzian and Gaussian peak-profile functions was employed to investigate the effects of calcination temperature on the crystallite size and lattice microstrain. The results demonstrated that the calcination temperature significantly affected the MgO nanoparticles. With increasing temperature, the microstrain decreased, the crystallite size increased, and the thermal stability and ordering of the lattice improved. The study also revealed that increasing the calcination temperature led to a significant increase in the unit-cell volume and lattice ordering. When comparing the Lorentzian and Gaussian profiles, it was observed that both profiles produced very similar effects on the crystallite size; however, their effects on strain were different. Therefore, it was concluded that the calcination temperature used during the synthesis of MgO nanoparticles has a direct effect on the crystallite size, defect concentration, and the structural quality of the final product.

Keywords: Magnesium oxide nanoparticles; calcination temperature; Williamson-Hall analysis; X-ray diffraction; crystallite size; lattice microstrain; defect evolution; nanocrystalline oxides.

DOI: https://doi.org/10.31349/RevMexFis.72.061006

1. Introduction

Magnesium oxide (MgO) nanoparticles have great potential for multiple applications due to their unique characteristics arising from their diverse physicochemical properties. Some applications of MgO nanomaterials include catalysis, optoelectronics, energy storage systems, refractory materials, antibacterial coatings, and biomedical engineering [1-3]. Compared with bulk materials, nanoscale MgO has a higher surface-to-volume ratio, a denser concentration of surface active sites, and defect-mediated functional properties. MgO nanoparticles exhibit enhanced catalytic, dielectric, and optical properties [4,5]. The microstructural characteristics of oxide nanoparticles are affected by the synthesis methods and heat treatments employed. The condensation and calcination of the oxide precursor are particularly important, as they can significantly alter the final microstructure of the nanoparticles by changing the concentration and morphology of surface defects [6-8]. Other factors also influence the microstructure of MgO nanoparticles, such as calcination temperature, which can affect the migration and diffusion of atoms and thereby reduce defects. Previous studies have shown that as the calcination temperature increases, crystallinity improves while both defect density and microstrain decrease until an optimal temperature is reached [9,10]. Beyond this point, higher calcination temperatures may lead to particle agglomeration and a reduction in active surface area, thereby decreasing particle efficiency [11].

MgO nanoparticles are useful for studying microstructural changes at elevated temperatures because of their simplicity and stability. MgO crystal structures contain defects that exhibit distinct behavioral features [12,13]. Therefore, precise measurements of the microstructural features of MgO nanostructures are essential to understanding the relationship among processing, structure, and material properties [14,15]. This is particularly important for parameters such as crystallite size, dislocation density, internal stress, and microstrain.Among the various techniques used to investigate nanocrystalline materials, X-ray Diffraction (XRD) is one of the most prominent. Traditionally, the Scherrer equation has been used to estimate crystallite size from the broadening of XRD peaks, often neglecting the contribution of internal strain [16,17]. In contrast, the Williamson-Hall (W-H) equation allows peak broadening to be decomposed into size and strain contributions [18]. The W–H method can be further improved through the use of Lorentzian or Gaussian peak-profile functions, which help distinguish the two broadening mechanisms. Furthermore, the W–H approach can be applied to describe defect behavior and structural relaxation in oxide materials [19-22].

Recently, extensive research has focused on the influence of calcination temperature on the properties of nanoscale ox-

ides, particularly Mg-based ferrites [23,24]. Mansouri and co-workers reported that chromium substitution in magnesium ferrites caused lattice distortion and defect engineering, thereby affecting both structural and optical properties of Mg–Co ferrite nanoparticles [25]. Zarai and colleagues observed that thermal treatment of $Mg_{0.6}Co_{0.4}FeAlO_4$ spinel ferrites enhanced crystallinity and optoelectronic properties while reducing the optical band gap [26]. Similarly, Chebbi and co-workers investigated the influence of chromium substitution and thermal treatment on the structural, optical, and electrical properties of Mg–Co ferrite nanoparticles [27]. Jdey and colleagues demonstrated that dielectric properties of Mg-based ferrites improved with enhanced lattice ordering, reduced microstrain, and higher calcination temperatures [17,28,29]. Numerous studies have also shown that thermal treatment of nanoscale oxides promotes hierarchical grain growth, reduction of lattice imperfections and structural defects, stress relaxation, and improved crystallinity quality and stability [30,31]. However, only a limited number of studies have focused specifically on MgO nanoparticles, and even fewer have investigated the relationship between calcination temperature, crystallite growth, lattice strain, and defect density [32]. Moreover, detailed Williamson-Hall analyses using both Lorentzian and Gaussian peak fitting methods remain scarce in studies concerning thermally treated MgO nanoparticles [25]. Understanding these parameters is essential for improving the application of MgO nanostructures in catalytic, optical, dielectric, and biomedical fields [17,33].

The present study investigates the effects of calcination temperature on the structure and microstructure of MgO nanoparticles synthesized using the co-precipitation method. MgO nanoparticles were prepared and calcined at different temperatures to evaluate the impact of calcination temperature on nanoparticle microstructure. The crystallite size and stress of the calcined MgO nanoparticles were analyzed using X-ray Diffraction (XRD), while Williamson-Hall (W–H) modeling methods were employed to estimate microstrain and dislocation density. Both Lorentzian and Gaussian peak-profile fitting methods were utilized in the W–H analysis. Additionally, the study evaluates the effects of synthesis methods on the thermal and microstructural properties of MgO nanoparticles prepared via co-precipitation. The Lorentzian and Gaussian methods were also used to explain peak-profile positioning and estimate crystallite size and microstrain. Finally, the study provides insights into microstructural stabilization and defect evolution in MgO nanomaterials.

2. Experimental details

2.1. Chemicals and materials

All chemicals used were of analytical grade, as this guarantees high purity MgO nanoparticle synthesis. Magnesium sulfate heptahydrate ($MgSO_4{\cdot}7H_2O$, $\geq$99%, Sigma-Aldrich) was used as the magnesium source for nanoparticle synthesis because of its convenient solubility. $MgSO_4{\cdot}7H_2O$ was selected because Mg^{2+} ions precipitate completely under alkaline conditions.As the precipitating agent, Ammonium Hydroxide (NH_4OH, analytical grade, Sigma-Aldrich) was employed to control the pH and facilitate the formation of magnesium hydroxide precipitates. Distilled water was used throughout the synthesis process in order to minimize side reactions and ionic contamination. The observed changes in the structural and microstructural properties of the MgO nanoparticles were attributed solely to the effects of calcination. This was ensured by taking utmost care to avoid the presence of precursor impurities during the synthesis process.

2.2. Synthesis of MgO Nanoparticles by co-precipitation method

The synthesis of MgO nanoparticles was carried out using a simple and effective controlled co-precipitation route. This method was selected because it offers low synthesis cost, high purity of the final product, and excellent control over the size and morphology of the nanoparticles. Magnesium sulfate heptahydrate ($MgSO_4 \cdot 7H_2O$, Sigma Aldrich, 99%) was used as the magnesium source. A measured quantity of $MgSO_4 \cdot 7H_2O$ was dissolved in 100 mL of freshly distilled water to prepare a 0.5 M magnesium precursor solution. The solution was stirred continuously at 700 rpm and heated to 80–90 °C for 24 h to ensure complete dissolution of the precursor salts. This process enabled uniform ion distribution within the solution and promoted homogeneous nucleation.To form magnesium hydroxide ($Mg(OH)_2$), ammonium hydroxide (NH_4OH, analytical grade, Sigma Aldrich) was used as the precipitation agent and added dropwise:

$$MgSO_4 + 2NH_4OH \rightarrow Mg(OH)_2 + (NH_4)_2SO_4$$

NH_4OH was used because it creates a controlled alkaline environment and sublimates during calcination, thereby keeping the final MgO product free from impurities. During the experiments, the reaction medium was maintained at an alkaline pH of approximately 10–11 to ensure complete precipitation of all Mg^{2+} ions as $Mg(OH)_2$ and to achieve a homogeneous particle-size distribution.The homogeneous white suspension obtained was centrifuged at 6000 rpm for 10 min, and the resulting precipitate was washed several times with distilled water to remove sulfate and ammonium ions. The $Mg(OH)_2$ precipitate was then dried at 100 °C for 12 h. This drying process was carried out to remove moisture and prepare the sample for subsequent calcination. The $Mg(OH)_2$ powder was calcined at different temperatures to obtain various morphologies and structural characteristics. Prior to calcination, the powder was finely ground to reduce agglomeration and promote a more homogeneous distribution of particles.

2.3. Calcination at different temperatures

The researchers divided the dried $Mg(OH)_2$ powder into three batches, which were then placed in high-purity alumina

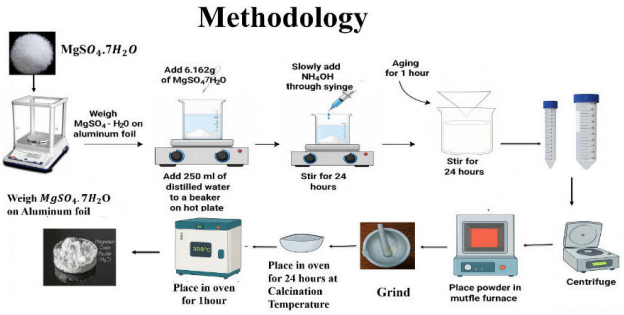


FIGURE 1. Schematic for the preparation steps followed for all samples preparation

crucibles to prevent contamination during thermal treatment. Each sample was then placed in a programmable muffle furnace to convert $Mg(OH)_2$ into MgO under an open-air atmosphere:

$$Mg(OH)_2 \rightarrow MgO + H_2O. \quad (1)$$

The calcination process was carried out at temperatures of 450 °C, 650 °C, and 700 °C using a controlled heating rate of 5 °C min^{-1}. An isothermal holding time of 24 h was maintained to ensure complete phase transformation and crystallization. The selected calcination temperatures were chosen to investigate the temperature-dependent structural evolution of MgO nanoparticles. The lower calcination temperature of 450 °C was used to examine the initial stage of crystallization, which generally results in smaller crystallite sizes and higher defect density. The higher calcination temperatures of 650 °C and 700 °C were selected to promote grain growth, lattice relaxation, reduction of structural defects, and improved lattice ordering. These temperatures also lie within the range reported in the literature where significant microstructural changes in MgO nanoparticles are commonly observed.After calcination, the furnace was allowed to cool naturally to room temperature in order to minimize thermal shock and prevent particle cracking. The obtained MgO powder samples were then gently ground to break weak agglomerates and stored in sealed glass containers to avoid moisture absorption.The samples were labeled as MgO-450, MgO-650, and MgO-700, respectively, and were further characterized using the Williamson-Hall (W-H) method to investigate their structural and microstructural properties.

2.4. X-Ray diffraction (XRD) characterization

To evaluate the impact of calcination temperature on MgO nanoparticles, X-ray Diffraction (XRD) analysis was performed. The analysis was carried out using a Philips X'Pert PRO X-ray diffractometer equipped with a Cu Kα radiation source. The X-ray source operated at 40 kV and 40 mA. Prior to analysis, the instrument accuracy was verified and calibrated using a commercial silicon standard.The XRD scans were recorded over an angular range of $10°$ to $80°$ with a step size of $0.02°$, a counting time of 1 s per step, and a scanning rate of $2°$ min^{-1}. The obtained diffraction patterns were indexed, and the Joint Committee on Powder Diffraction Standards (JCPDS) database was used to identify the periclase phase of MgO and confirm the complete removal of secondary phases from the calcined $Mg(OH)_2$ products.The diffraction peak broadening was analyzed using Line Profile Analysis (LPA) with combined Lorentzian and Gaussian peak-profile fitting approaches. LPA was employed because it provides reliable estimations of crystallite size and microstrain-induced broadening effects within the samples. Line profile analysis and peak broadening techniques are widely applied in the microstructural characterization of nanostructured materials.

2.5. Williamson-Hall method

The Williamson-Hall (W-H) method is used to evaluate the broadening of X-ray diffraction peaks caused by finite crystallite size and lattice microstrain. Assuming the strain is uniform and anisotropic, the total peak broadening (β) can be expressed using the Williamson-Hall equation as follows:

$$\beta \cos\theta = \frac{k\lambda}{D} + 4\epsilon \sin\theta, \quad (2)$$

where β is the full width at half maximum (FWHM) of the diffraction peak after instrumental correction, k is the shape factor ($k = 0.94$), λ is the X-ray wavelength, D is the crystallite size, ϵ is the uniform elastic microstrain of the crystal, and θ is the Bragg diffraction angle. In this equation, $k\lambda/D$ represents size broadening, whereas $4\epsilon \sin\theta$ corresponds to strain broadening.In the Williamson-Hall analysis, the FWHM values of the most intense diffraction peaks corresponding to different crystallographic planes were extracted from the corrected XRD patterns after removing instrumental broadening. The quantities $\beta\cos\theta$ and $4\sin\theta$ were linearly fitted to separate the contributions of crystallite size and lattice strain. The crystallite size was determined from the intercept of the fitted line, while the lattice microstrain was obtained from the slope.This method enables the quantitative determination of crystallite size and lattice imperfections in MgO nanoparticles synthesized at different calcination temperatures and further characterized using thermal analysis [34].

3. Results and discussion

3.1. XRD analysis

The X-ray diffraction (XRD) patterns of MgO nanoparticles calcined at 450 °C, 650 °C, and 700 °C (Fig. 2) reveal significant structural evolution with increasing calcination temperature. The diffraction peaks observed at approximately $2\theta \approx 36.9°$, $42.8°$, and $62.1°$ correspond to the (111), (200), and (220) crystallographic planes of cubic periclase MgO, respectively. These results are consistent with JCPDS/PDF card No. 45–0946 and previously reported MgO diffraction studies [25,35,36]. The absence of secondary impurity peaks confirms the formation of phase-pure MgO nanoparticles.

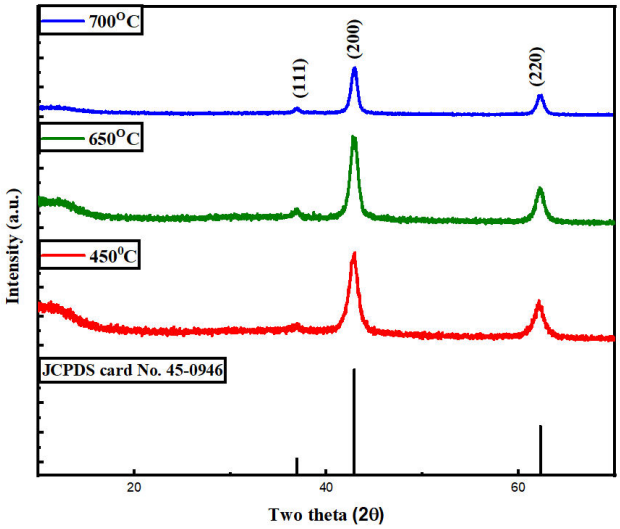


FIGURE 2. XRD patterns of MgO nanoparticles at different calcination temperatures (JCPDS No. 45-0946).

Similar calcination-temperature-dependent structural behavior has also been reported for MgO-based nanomaterials and spinel ferrite systems [25,26,28,37]. At a calcination temperature of 450 °C, the diffraction peaks are relatively broad with lower intensity, indicating smaller crystallite size, lower crystallinity, and higher lattice microstrain. Peak broadening is generally associated with lattice distortion, structural defects, and incomplete crystallization resulting from insufficient thermal energy during heat treatment [35,36]. The restricted atomic mobility at lower temperatures suppresses crystallite growth and enhances internal lattice strain. Similar observations have been reported for Mg-based ferrite systems [24,25]. With increasing calcination temperature to 650 °C and 700 °C, the diffraction peaks become sharper and more intense, indicating improved crystallinity and enhanced structural ordering. The increased thermal energy promotes atomic diffusion, lattice relaxation, and grain growth, thereby reducing defect density and lattice strain [28,36]. Grain growth occurs through the coalescence of smaller crystallites into larger grains in order to minimize the total grain boundary energy. Similar improvements in structural ordering and crystallinity at elevated temperatures were also reported by Zarai *et al.* [26], Jdey *et al.* [38], and Harrabi *et al.* [37] for Mg-based spinel ferrite systems. Unlike previous studies mainly focused on structural, optical, and dielectric enhancements, the present work systematically correlates crystallite growth, lattice strain reduction, and lattice expansion with calcination temperature using Williamson-Hall analysis. A gradual shift of the diffraction peaks toward lower 2θ values was observed with increasing calcination temperature. According to Bragg's law,

$$n\lambda = 2d\sin\theta, \tag{3}$$

the decrease in 2θ values indicates an increase in interplanar spacing (d-spacing), suggesting lattice expansion within the cubic MgO structure. The crystallographic parameters summarized in Table I further confirm this trend, where the lattice parameter increased from 4.214 Å to 4.229 Å, while the unit cell volume increased from 74.84 Å^3 to 75.64 Å^3 as the calcination temperature increased from 450 °C to 700 °C. The observed lattice expansion may be attributed to thermally induced defect relaxation and structural reorganization within the MgO lattice [28,36,39].

TABLE I. Crystallographic parameters of MgO nanoparticles at varying calcination temperatures, derived from XRD analysis of the (200) reflection, including diffraction angle (2θ), interplanar spacing (d), lattice parameter (a), and unit cell volume (V).

Parameters	450 °C	650 °C	700 °C
$2\theta_{(200)}$ (deg.)	42.8854	42.8063	42.7273
d-spacing, d (Å)	2.1071	2.1108	2.1146
Lattice parameter, a (Å)	4.2142	4.2216	4.2291
Unit cell volume, V (Å^3)	74.8431	75.2390	75.6387

With increasing calcination temperature, the (200) diffraction peak shifted toward lower 2θ values, indicating lattice expansion in cubic MgO. The data presented in Table I show that the interplanar spacing (d-spacing) increased from 2.1071 Å to 2.1146 Å. A slight increase in the lattice parameter and unit-cell volume was also observed, suggesting reduced lattice distortion and improved structural ordering.These changes in the crystallographic parameters are consistent with findings reported in the literature. Previous studies have shown that higher calcination temperatures enhance the structural stability of MgO nanoparticles and improve lattice uniformity due to defect reduction and lattice relaxation [37,40-45].

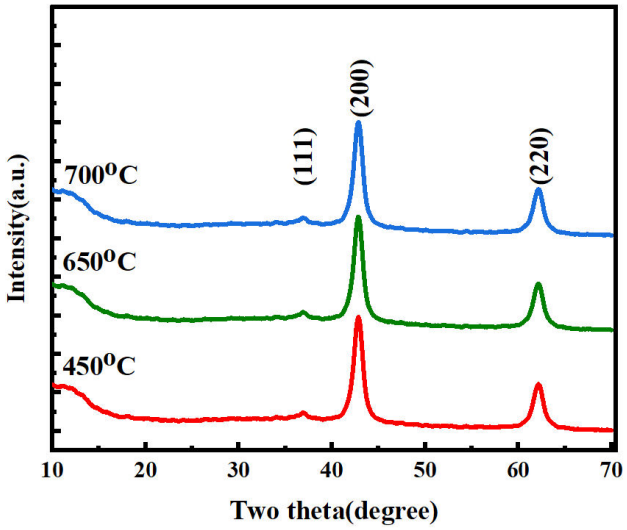


FIGURE 3. XRD patterns of MgO nanoparticles calcined at 450-700°C, showing a (200) peak shift to lower 2θ from lattice expansion and strain relaxation (FCC MgO, JCPDS 45-0946).

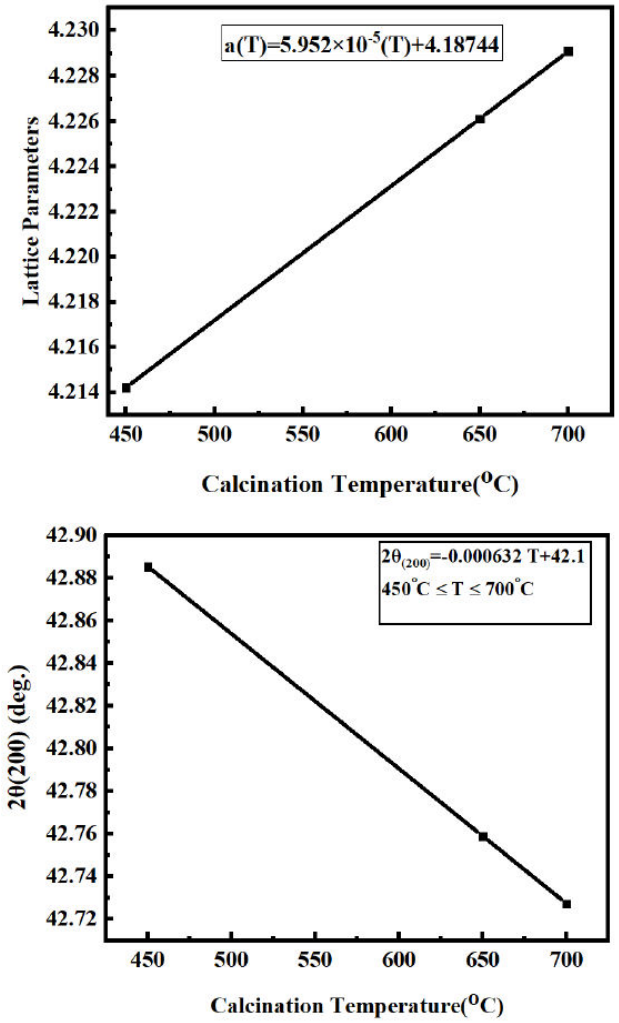


FIGURE 4. Systematic shift of the (200) diffraction peak toward lower angles and corresponding linear increase of the lattice parameter with calcination temperature, confirming thermally induced expansion of the MgO cubic lattice.

3.2. Lattice parameters

The lattice parameter was determined using the cubic relation

$$a = d\sqrt{(h^2 + k^2 + l^2)}, \tag{4}$$

in Fig. 4 show that X-ray diffraction (XRD) on MgO nanoparticles calcined at 450 °C, 650 °C, and 700 °C suggested the high crystallinity single-phase FCC structure (JCPDS 45-0946) formation [46]. With the increase in calcination temperature, the (200) diffraction peak shifted towards lower 2θ values which indicated that the lattice of cubic MgO was expanded. As noted, the d-spacing increased from 2.1071 Å to 2.1146 Å. Similarly, the lattice parameter increased from 4.2142 Å to 4.2291 Å, and the unit-cell volume was noted to increase from 74.843 Å^3 to 75.639 Å^3 and calcination temperature increased. This increase in the temperature showed that the lattice was less and less distorted and more and more ordered. This is in agreement with other studies that noted that as the temperature of calcined MgO nanoparticles was increased, the MgO nanoparticles remained thermally stable, and that the uniformity and stability of the MgO nanoparticles' lattice were improved [37,39,44,47]. Most of these studies focused on the fabrication of MgO and the improvement of the MgO's functional properties, as well as the degree of crystallinity of the MgO; however, little consideration was made to the relationship of the lattice parameters and the microstructural behavior of the MgO. The current study for MgO suggested a temperature-dependent XRD analysis of crystallographic parameters, a comparative analysis for MgO, and provided MgO lattice behavior.

From Table I and Fig. 4, the diffraction angle (2θ) corresponding to the (200) plane decreased systematically from $42.08°$ at 450 °C to $41.67°$ at 700 °C, while the corresponding lattice parameter increased from 4.187 Å to 4.192 Å, indicating lattice expansion with increasing calcination temperature. The relationship is given by:

$$2\theta_{(200)} = -0.000565\,T + 43.145. \tag{4}$$

Similarly, the corresponding linear increase in the lattice parameter with temperature follows:

$$a(T) = 5.952 \times 10^{-5}T + 4.18744,$$
$$450°\text{C} \leq T \leq 700°\text{C}. \tag{5}$$

The decrease in 2θ values and expansion of the lattice parameter are indicative of the thermal relaxation of the MgO lattice and thermal expansion of the crystal structure. This behavior is associated with the reduction of lattice defects and distortion at elevated calcination temperatures [41]. The linear relationship between lattice parameter and calcination temperature indicates that thermal treatment induces predictable changes in lattice dimensions in accordance with Vegard's law. This phenomenon has also been observed in MgO nanocrystals, where increasing calcination temperature resulted in improved crystallinity, reduced lattice defects and distortion, and lattice expansion [48,49].

3.3. Nelson–Riley method

The Nelson–Riley extrapolation method was employed to determine the accurate lattice parameter by minimizing systematic errors associated with X-ray diffraction measurements. The Nelson–Riley function is expressed as

$$f(\theta) = \frac{1}{2}\left(\frac{\cos^2\theta}{\sin\theta} + \frac{\cos^2\theta}{\theta}\right), \tag{6}$$

where θ is the Bragg angle expressed in radians according to the method proposed by Nelson and Riley [50]. The true lattice parameter was obtained by linear extrapolation of the apparent lattice parameter to $f(\theta) = 0$, thereby minimizing systematic errors arising from specimen displacement, sample transparency, and instrumental effects.

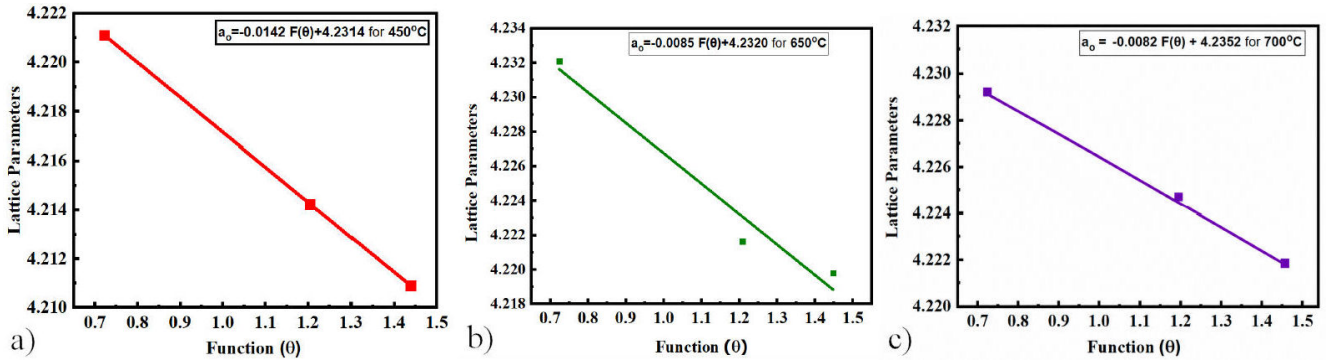


FIGURE 5. Nelson-Riley plot for MgO nanoparticles calcined at 450°C, 650 °C, and 700 °C.

The corresponding Nelson–Riley plots for MgO nanoparticles calcined at 450, 650, and 700°C are presented in Figs. 5a) – 5c). The extrapolated lattice parameter increased from 4.2314 Å at 450°C to 4.2352 Å at 700°C, indicating lattice strain relaxation, improved crystallinity, and enhanced crystal ordering. The excellent linearity observed for all three temperatures confirms the consistency of the diffraction data and the applicability of the Nelson–Riley method for accurate lattice parameter determination.

The gradual increase in the extrapolated lattice parameter with increasing calcination temperature is attributed to the reduction of lattice imperfections, relaxation of residual microstrain, and thermally assisted grain growth. As the calcination temperature increases, atomic diffusion becomes more effective, allowing Mg^{2+} and O^{2-} ions to occupy energetically favorable lattice positions, thereby reducing defect concentration and improving long-range structural ordering.

Furthermore, the intercept values obtained from the linear fits are in close agreement with the lattice expansion trend observed from the XRD analysis, providing independent confirmation of the structural evolution induced by calcination. The consistent increase in lattice parameter also supports the crystallite size enhancement and strain relaxation obtained from the Williamson–Hall analysis, indicating that higher calcination temperatures promote the formation of well-crystallized MgO nanoparticles with improved structural stability [22,36].

3.4. Microstructural parameters analysis

Crystallite size and microstrain are critical factors in determining the microstructural and physical properties of materials. X-ray diffraction (XRD) line profile analysis is among the most reliable methods for estimating crystallite size and the non-uniform lattice strain arising from atomic displacements relative to ideal lattice positions [51]. The broadening of diffraction peaks corresponding to a given (hkl) reflection is mainly attributed to finite crystallite size and lattice strain induced during partial crystallization. For samples exhibiting multiple diffraction peaks, as in the present study, the Williamson-Hall (W-H) method is considered the most appropriate approach [52]. The integral breadth (area-normalized peak width) of each diffraction peak was determined experimentally. The observed peak broadening (B) contains contributions from instrumental effects (b), crystallite size, and microstrain.To obtain physically meaningful microstructural parameters, instrumental broadening must first be corrected using a standard crystalline reference sample.

Instrumental Broadening Correction:

Depending on the assumed peak profile, two different correction approaches are used:

(1) **Gaussian peak profile (strain-dominated broadening):**

$$\beta = \sqrt{B^2 - b^2}. \tag{7a}$$

This quadratic subtraction is valid when peak shapes follow a Gaussian distribution, where broadening contributions are statistically independent.

(2) **Lorentzian (Cauchy) peak profile (size-dominated broadening):**

$$\beta = B - b. \tag{7b}$$

This linear subtraction is appropriate when peak broadening follows a Lorentzian shape, typically associated with finite crystallite size effects. Here, β represents the corrected integral breadth after removing instrumental contribution. After instrumental correction, the total physical broadening can be expressed as the sum of size and strain contributions:

$$\beta_{\text{hkl}} = \beta_{\text{size}} + \beta_{\text{strain}} + \beta_{\text{inst}}. \tag{8}$$

After correction:

$$\beta_{\text{corr}} = \begin{cases} \sqrt{B^2 - b^2}, & \text{(Gaussian assumption)}, \\ B - b, & \text{(Lorentzian assumption)}. \end{cases} \tag{9}$$

For further analysis using the Williamson-Hall method, the corrected broadening is separated into size and strain components:

$$\beta_{\text{corr}} = \beta_{\text{size}} + \beta_{\text{strain}}, \tag{10}$$

or, in squared form for Gaussian-type analysis:

$$\beta^2_{\text{corr}} = \beta^2_{\text{size}} + \beta^2_{\text{strain}}. \tag{11}$$

3.5. Williamson-Hall equation

The Williamson-Hall (W-H) method separates size- and strain-induced broadening by plotting peak broadening against diffraction angle. It relates total broadening (β) to crystallite size (D) and microstrain (ε) [53]:

$$\beta = \frac{k\lambda}{D\cos\theta} + 4\varepsilon\tan\theta, \tag{12}$$

$$\beta\cos\theta = \frac{k\lambda}{D} + 4\varepsilon\sin\theta. \tag{13}$$

For Gaussian approximation, the squared form is:

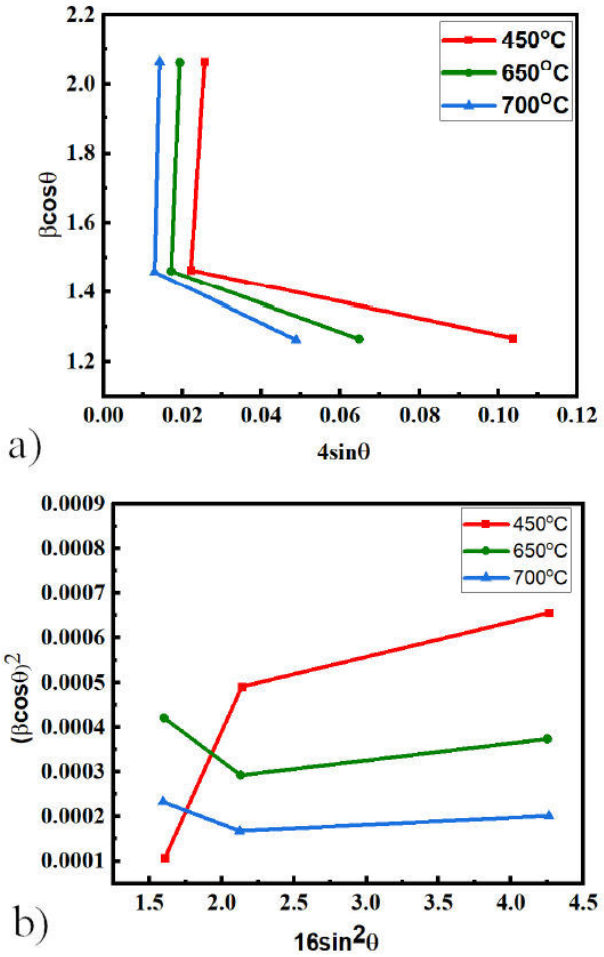


FIGURE 6. Williamson–Hall plots of MgO nanoparticles calcined at 450, 650, and 700°C: a) Lorentzian W–H plots of $\beta\cos\theta$ versus $4\sin\theta$, and b) Gaussian squared-form W–H plots of $(\beta\cos\theta)^2$ versus $16\sin^2\theta$, showing the effect of calcination temperature on crystallite size and lattice microstrain.

$$\beta^2\cos^2\theta = \left(\frac{k\lambda}{D}\right)^2 + 16\varepsilon^2\sin^2\theta, \tag{14}$$

where β is the full width at half maximum (FWHM) after instrumental correction (in radians), θ is the Bragg diffraction angle, k is the shape factor ($k = 0.94$), λ is the X-ray wavelength, D is the crystallite size, and ε is the microstrain. The Williamson-Hall (W-H) analysis was conducted to investigate the effect of calcination temperature on the crystallite size and lattice strain of MgO nanoparticles synthesized at 450 °C, 650 °C, and 700 °C (Fig. 6). The plots of $\beta\cos\theta$ versus $4\sin\theta$ and $(\beta\cos\theta)^2$ versus $16\sin^2\theta$ revealed that increasing calcination temperature resulted in larger crystallite size and lower lattice microstrain. At 450 °C, the W-H plots exhibited a higher slope and smaller intercept, indicating significant lattice strain and smaller crystallite size due to incomplete crystallization, lattice distortion, and defect-rich grain boundaries [53]. Limited atomic diffusion at lower calcination temperatures restricts crystallite growth and promotes structural disorder. With increasing calcination temperature to 650 °C and 700 °C, the slope of the W-H plots decreased while the intercept increased, confirming progressive strain relaxation and crystallite growth. Enhanced thermal diffusion at elevated temperatures promotes atomic rearrangement within the MgO lattice, reducing defect density and improving structural ordering. Similar behavior has been reported for Mg-based nanomaterials [26,54]. At 700 °C, the W-H analysis showed the lowest microstrain and the largest crystallite size, indicating improved lattice stability and enhanced long-range atomic ordering. These results demonstrate that calcination temperature plays a critical role in controlling the microstructural evolution and structural quality of MgO nanoparticles.

The Williamson-Hall (W-H) analysis shows that both Lorentzian and Gaussian fittings indicate that crystallite size and lattice microstrain depend on calcination temperature (Fig. 7). For samples calcined at 450 °C, the crystallite sizes were 5.9 nm (Lorentzian) and 6.5 nm (Gaussian). Correspondingly, the microstrain values were recorded as 3.7×10^{-3} and 0.91×10^{-3}. The relatively high crystallite size and large microstrain indicate incomplete crystallization and lattice distortion due to a high defect density, primarily caused by insufficient atomic diffusion during densification.The microstrain and crystallite size were observed to change with calcination temperature. At 650 °C, the values were 2.82×10^{-3} (microstrain, Lorentzian) and 7.5 nm (crystallite size), while for Gaussian fitting the corresponding values were 0.71×10^{-3} and 8.3 nm. Similar temperature-dependent grain growth and strain reduction have also been reported by Chebbi *et al.* for Mg-based ferrite nanomaterials. Contrarily, most studies focus primarily on crystallinity improvement, whereas the present study correlates crystallite growth and W-H microstrain using both Lorentzian and Gaussian fittings of the W-H model. At 700 °C, the crystallite sizes increased to approximately 10.0 nm (Lorentzian)

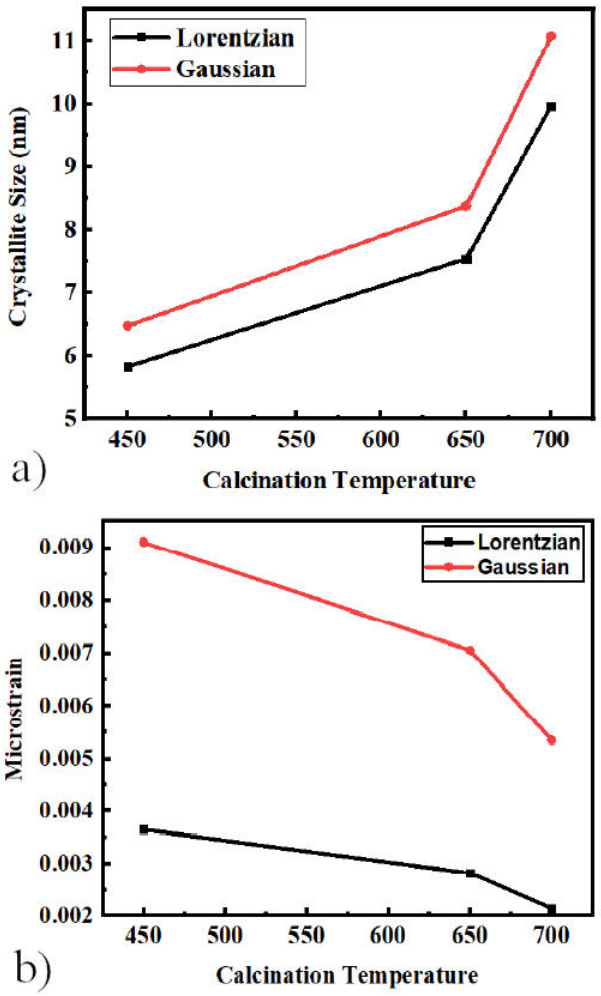


FIGURE 7. Williamson-Hall analysis of MgO nanoparticles showing a) average crystallite size versus calcination temperature and b) microstrain change with calcination temperature based on Lorentzian and Gaussian profile fittings.

and 11.0 nm (Gaussian), while the microstrain values significantly decreased to 2.1372×10^{-3} and 0.5343×10^{-4}, respectively. The increase in crystallite size and reduction in strain confirm thermally induced grain coalescence, reduced defect concentration, and improved atomic ordering. Similar phenomena have also been reported by Pathak *et al*. for nanomaterials [55]. Overall, the W-H analysis shows that the observed trend is consistent with increased crystallinity and structural stability of MgO nanoparticles, accompanied by internal stress reduction and improved lattice ordering.

3.6. Intrinsic surface stress

Intrinsic surface stress reflects the influence of lattice distortion and surface effects on the structural stability of MgO nanoparticles. Following the reported methodology, the intrinsic surface stress was estimated using [56]

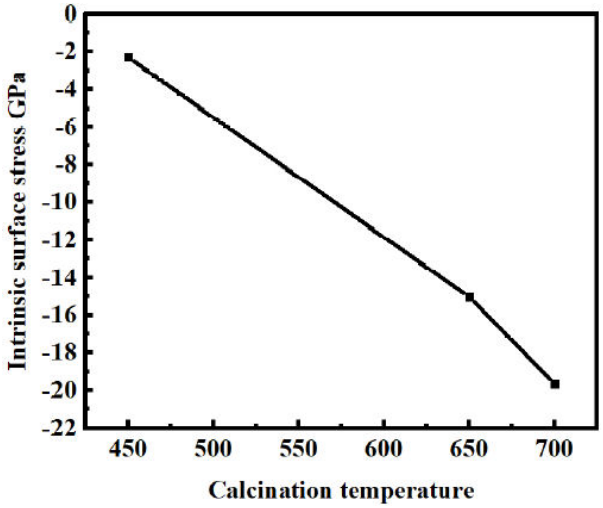


FIGURE 8. Variation of intrinsic surface stress of MgO nanoparticles as a function of calcination temperature.

$$\sigma = \frac{Y}{2\gamma}\left(\frac{a_0 - a}{a_0}\right), \tag{16}$$

where σ is the intrinsic surface stress, Y is the Young's modulus, γ is the Poisson's ratio, a_0 is the strain-free lattice parameter of bulk MgO, and a is the measured lattice parameter. The term $(a_0 - a)/a_0$ represents the relative lattice distortion. Since Y is expressed in GPa, while γ and $(a_0 - a)/a_0$ are dimensionless, the calculated intrinsic surface stress is also expressed in GPa. Negative values of α indicate compressive surface stress, whereas positive values correspond to tensile surface stress.

Figure 8 illustrates the variation of intrinsic surface stress with calcination temperature. The intrinsic surface stress becomes progressively more negative with increasing calcination temperature, indicating an increase in the magnitude of compressive surface stress. At 450 °C, the intrinsic surface stress is approximately -2.30 GPa, which is associated with incomplete crystallization, limited atomic diffusion, and a relatively high concentration of lattice defects. Increasing the calcination temperature to 650 °C results in a larger compressive stress of approximately -15.0 GPa due to improved lattice ordering and defect reduction. At 700 °C, the intrinsic surface stress reaches approximately -19.8 GPa, indicating enhanced grain densification, improved atomic packing, and greater structural stability. The progressive increase in compressive intrinsic surface stress demonstrates that calcination promotes lattice stabilization and improves the crystallinity of MgO nanoparticles [57].

The crystallographic Young's modulus was estimated from the intrinsic surface stress and the average microstrain using

$$E(\text{hkl}) = \frac{\sigma}{\langle\varepsilon\rangle}, \tag{15}$$

where σ is the intrinsic surface stress calculated using Eq. (16), and $\langle\varepsilon\rangle$ is the average microstrain obtained from the

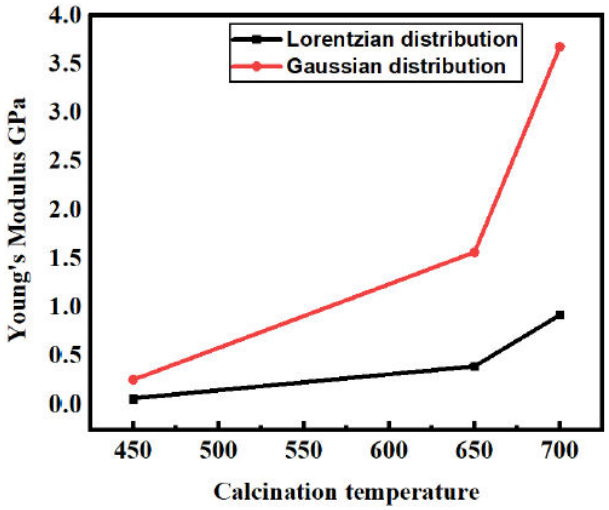


FIGURE 9. Variation of crystallographic Young's modulus of MgO nanoparticles obtained from Lorentzian and Gaussian Williamson–Hall analyses.

Williamson–Hall analysis [36]. The calculated values of $E(hkl)$ for each calcination temperature are presented in Fig. 9. These values provide information about the elastic response of the crystallographic planes.

Figure 9 shows the variation of Young's modulus with calcination temperature for both Lorentzian and Gaussian distributions. In both fitting methods, Young's modulus increases with increasing calcination temperature, indicating an enhancement in the elastic stiffness of the MgO nanoparticles. The Lorentzian values increase from 0.0631 to 0.9191 GPa, whereas the Gaussian values increase from 0.2523 to 3.6766 GPa as the calcination temperature increases from 450 to 700 °C. The higher values obtained from the Gaussian fitting indicate greater sensitivity to microstructural evolution. The increase in Young's modulus is consistent with the improvement in crystallinity, reduction of lattice defects, and enhanced atomic ordering produced by high-temperature calcination [58].

Table II summarizes the Williamson–Hall parameters of MgO nanoparticles. Increasing the calcination temperature results in a gradual increase in crystallite size and a corresponding decrease in lattice microstrain and dislocation density for both Lorentzian and Gaussian analyses. The reduction in microstrain and defect density indicates progressive lattice relaxation and improved structural ordering. These microstructural changes are accompanied by an increase in the magnitude of compressive intrinsic surface stress and an increase in Young's modulus, confirming that high-temperature calcination enhances the structural stability and elastic response of MgO nanoparticles [36,38].

TABLE II. Williamson–Hall parameters of MgO nanoparticles at different calcination temperatures.

Temp. (°C)	D_L (nm)	D_G (nm)	ε_L ($\times 10^{-3}$)	ε_G ($\times 10^{-3}$)	δ ($\times 10^{14}$ m^{-2})
450	5.8266	6.4741	3.6433	0.9108	22.256
650	7.5357	8.3730	2.8218	0.7054	13.305
700	9.9681	11.0757	2.1372	0.5343	7.605

3.7. Lattice strain estimation

Strain is the change in dimensions of a sample compared to its original length and can be either constant or irregular. Isotropic expansion or contraction of a unit cell, shifting XRD peaks without broadening, is due to uniform strain. Non-uniform strain, which is caused by defects, deformation, and incomplete crystallization, shifts atoms in an irregular manner and causes broadening of XRD peaks [59]. This strain is often expressed as:

$$\text{Lattice Strain} = \frac{\Delta a}{a_0}. \tag{16}$$

Here, Δa represents the deviation of the lattice parameter from the strain-free reference state a_0, which is taken as the equilibrium lattice parameter in the absence of applied stress or thermal strain. Lattice strain is associated with variations

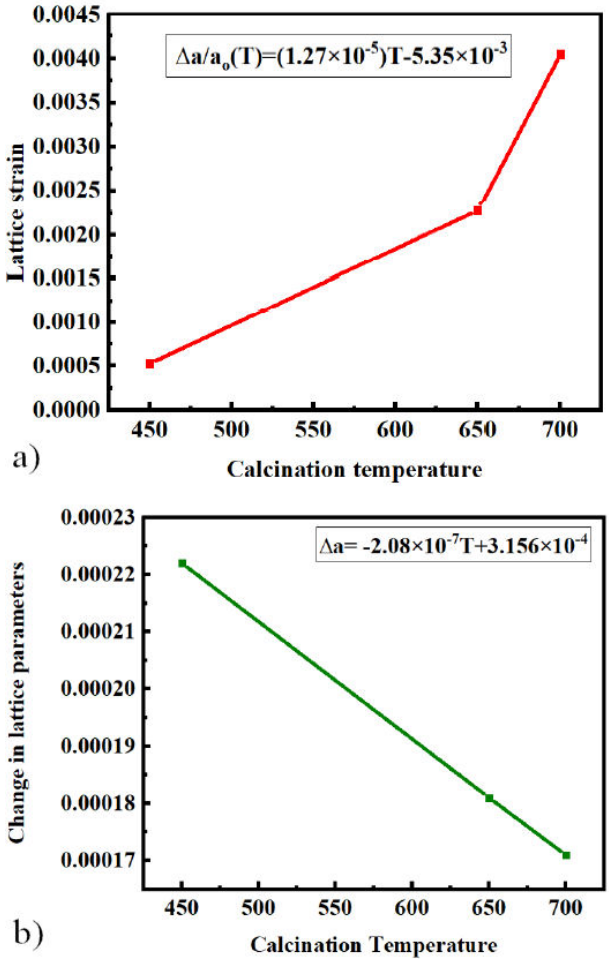


FIGURE 10. Variation of lattice strain ($\Delta a/a_0$) with calcination temperature for MgO nanoparticles.Evolution of the lattice parameter deviation (Δa) with calcination temperature.

in the lattice parameter ratio ($\Delta a/a_0$). Figure 10 shows that the lattice strain of MgO nanoparticles decreases progressively with increasing calcination temperature. The higher strain observed at 450 °C is attributed to incomplete crystallization, smaller crystallite size, and structural disorder due to lattice defects. Limited thermal energy at lower temperatures restricts atomic diffusion and lattice rearrangement, resulting in increased internal strain. At higher calcination temperatures (650 °C and 700 °C), enhanced thermal diffusion promotes crystallite growth and lattice relaxation, leading to reduced microstrain and improved structural ordering [60,61]. The Williamson-Hall analysis further indicates that increasing calcination temperature causes a slight increase in lattice deformation parameter (Δa), suggesting thermally induced lattice expansion and structural stabilization of the cubic MgO phase, as shown in Fig. 10. These results confirm that elevated calcination temperatures reduce lattice defects and improve the structural stability of MgO nanoparticles.

3.8. Dislocation density

Dislocation density refers to the total length of dislocation lines per unit volume and is an important parameter for defining structural imperfections in nanocrystalline materials. A high dislocation density indicates significant internal strain, lattice distortion, and low crystallinity. A reduced dislocation density indicates improved crystallinity, better structural ordering, and reduced lattice defects. The dislocation density (ρ) can be calculated from the Williamson-Smallman relation:

$$\rho = \frac{15\,\varepsilon}{aD}, \tag{17}$$

where ε represents the microstrain obtained from Williamson-Hall analysis, a denotes the lattice parameter, and D signifies the crystallite size. The equation incorporates both strain and crystallite size, thus enabling a more precise estimation of the defect density in strained nanomaterials.

As shown in Fig. 11, dislocation density for MgO nanoparticles decreases with an increase in calcination temperature and is observed for both Lorentzian and Gaussian distributions. Dislocation density is highest at 450 °C owing to the small crystallite size, high internal strain, and incomplete lattice ordering resulting from low-temperature calcination [62]. Calcination temperatures of 650 °C and 700 °C promote greater atomic ordering and grain growth, which leads to reduced lattice distortion and consequently a decrease in dislocation density, indicating improved structural and crystalline quality of MgO nanoparticles. This also confirms enhanced structural stability at higher temperatures. The Lorentzian profile shows higher dislocation density than the Gaussian profile, indicating that Lorentzian fitting corresponds to higher strain and more pronounced peak broadening compared to Gaussian fitting. A similar decrease in dislocation density and lattice defects with increasing calcination temperature has been reported for Cr-substituted Mg-Co

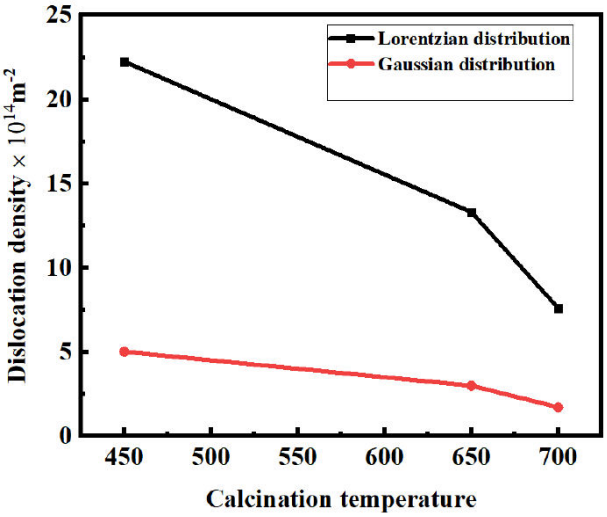


FIGURE 11. Variation of dislocation density (ρ) with calcination temperature for MgO nanoparticles, calculated using Lorentzian and Gaussian profiles via the Williamson-Smallman method.

ferrites by Chebbi *et al.* [25]. This was attributed to grain growth, strain relaxation, and improved structural ordering at higher temperatures. Jdey *et al.* [28] reported similar behavior in $Mg_{0.6}Cu_{0.4}FeCrO_4$ ferrites, while Harrabi *et al.* [37] demonstrated improved lattice stability and enhanced grain boundary coherence in Mg-Co-Cu ferrites at elevated calcination temperatures.Most of these studies focused on substituted ferrite systems with complex magnetic, electrical, and cation distribution effects, making interpretation of pure strain-driven systems more challenging. In contrast, the present work focuses on structurally simple cubic MgO nanoparticles, analyzing thermally induced defect evolution using comparative Lorentzian and Gaussian Williamson-Hall analysis [63]. The study demonstrates that increasing calcination temperature reduces lattice defects, enhances structural ordering, and improves the microstructural stability of MgO nanoparticles. The comparative analysis shows that present MgO nanoparticles and previously reported Mg-based ferrite systems have a lot in common. In those systems, higher calcination temperatures resulted in larger crystallite sizes, smaller lattice strains, and fewer defects due to thermally activated diffusion. Unlike ferrite materials that have complex structures and magnetic and cation distribution, our study focuses on MgO cubic nanoparticles, which have simpler structures. Our research also compares Lorentzian and Gaussian Williamson-Hall methods to evaluate thermally induced size-strain evolution.

4. Conclusion

This paper investigates the synthesis and post-synthesis characterization of MgO nanoparticles. MgO nanoparticles were synthesized via the co-precipitation method, followed by a post-synthesis morphology control procedure. The structural

and microstructural changes of the calcined samples were analyzed using X-ray diffraction (XRD), confirming the formation of a cubic single-phase MgO structure.Peak broadening observed in the XRD patterns indicates the presence of nanoscale crystallites, which were quantitatively analyzed using the Williamson-Hall (W-H) method. The W-H analysis reveals that calcination temperature significantly influences crystallite size and leads to a reduction in lattice microstrain, dislocation density, and structural defects through enhanced grain growth and strain relaxation mechanisms.Post-calcination XRD analysis at room temperature reveals that the crystallite size increases from 5–6 nm at 450 °C to 10–11 nm at 700 °C. Improved atomic ordering at elevated temperatures is further evidenced by shifts in XRD peak positions, indicating an increase in lattice parameter and unit-cell volume. Further analysis using Lorentzian and Gaussian peak fitting confirms these structural changes and supports the observed enhancement in crystallographic ordering. This study establishes a clear relationship between calcination temperature and crystallite size, defect concentration, and structural stability of MgO nanoparticles.The Williamson-Hall method is highlighted as a powerful tool for evaluating microstructural transformations in MgO nanomaterials. Overall, the results demonstrate that controlled calcination is an effective approach for tailoring the crystallite size, lattice strain, defect concentration, and structural stability of MgO nanoparticles for advanced functional applications.

1. M. S. Chavali and M. P. Nikolova, Metal oxide nanoparticles and their applications in nanotechnology, *SN applied sciences*, **1** (2019) 607.
2. Y. Yoon, P. L. Truong, D. Lee, and S. H. Ko, Metal-oxide nanomaterials synthesis and applications in flexible and wearable sensors, *ACS Nanoscience Au*, **2** (2021) 64-92.
3. N. Baig, I. Kammakakam, and W. Falath, Nanomaterials: A review of synthesis methods, properties, recent progress, and challenges, *Materials advances*, **2** (2021) 1821.
4. E. S. Araújo, M. F. Pereira, G. M. da Silva, G. F. Tavares, C. Y. Oliveira, and P. M. Faia, A review on the use of metal oxide-based nanocomposites for the remediation of organic-scontaminated water via photocatalysis: fundamentals, bibliometric study and recent advances, *Toxics*, **11** (2023) 658.
5. A. Dey, Semiconductor metal oxide gas sensors: A review, *Materials science and Engineering: B*, **229** (2018) 206.
6. B. Saruhan, R. Lontio Fomekong, and S. Nahirniak, Influences of semiconductor metal oxide properties on gas sensing characteristics, *Frontiers in Sensors*, **2** (2021) 657931.
7. A. Asghar, K. Khan, O. Hakami, W. M. Alamier, S. K. Ali, T. Zelai, M. S. Rashid, A. K. Tareen, and E. A. Al-Harthi, Recent progress in metal oxide-based electrode materials for safe and sustainable variants of supercapacitors, *Frontiers in Chemistry*, **12** (2024) 1402563.
8. D. Dong, S. S. Dhanabalan, P. F. M. Elango, M. Yang, S.Walia, S. Sriram, and M. Bhaskaran, Emerging applications of metaloxide thin films for flexible and stretchable electronic devices, *Applied Physics Reviews*, **10** (2023).
9. A. M. Negrescu, M. S. Killian, S. N. Raghu, P. Schmuki, A. Mazare, and A. Cimpean, Metal oxide nanoparticles: review of synthesis, characterization and biological effects, *Journal of Functional Biomaterials*, **13** (2022) 274.
10. M. G. Kim, J. M. Kang, J. E. Lee, K. S. Kim, K. H. Kim, M. Cho, and S. G. Lee, Effects of calcination temperature on the phase composition, photocatalytic degradation, and virucidal activities of TiO2 nanoparticles, *ACS Omega*, **6** (2021) 10668.
11. M. Rabiei, A. Palevicius, A. Dashti, S. Nasiri, A. Monshi, A. Doustmohammadi, A. Vilkauskas, and G. Janusas, Xray diffraction analysis and williamson-hall method in USDM model for estimating more accurate values of stress-strain of unit cell and super cells of hydroxyapatite, confirmed by ultrasonic pulse-echo test, *Materials*, **14** (2021) 2949.
12. J. Hornak, P. Trnka, P. Kadlec, O. Michal, V. Mentlík, P. Šutta, G. M. Csányi, and Z. A. Tamus, Magnesium oxide nanoparticles: dielectric properties, surface functionalization and improvement of epoxy-based composites insulating properties, *Nanomaterials*, **8** (2018) 381.
13. M.-A. Gatou, E. Skylla, P. Dourou, N. Pippa, M. Gazouli, N. Lagopati, and E. A. Pavlatou, Magnesium oxide (MgO) nanoparticles: synthetic strategies and biomedical applications, *Crystals*, **14** (2024) 215.
14. S. E. Elashery, I. Ibrahim, H. Gomaa, M. M. El-Bouraie, I. A. Moneam, S. S. Fekry, and G. G. Mohamed, Comparative study of the photocatalytic degradation of crystal violet using ferromagnetic magnesium oxide nanoparticles and MgO-bentonite nanocomposite, *Magnetochemistry*, **9** (2023) 56.
15. M. Ludwig *et al*., Corrosion resistance of MgO,based refractory raw materials to pbo-rich cu slag determined by hot-stage microscopy and pellet corrosion test, *Materials*, **15** (2022) 725.
16. L. M. Al-Harbi, M. Ezzeldien, A. A. Elhenawy, and A. H. Said, Assessment of the bioactivity of bioinspired magnesium oxide nanoparticles from the azadirachta indica extract, *Frontiers in Bioengineering and Biotechnology*, **12** (2024) 1480694.
17. X. Li, J. Zhao, X. Hong, Y. Yang, X. Tang, Y. Zhu, and T. Li, Calcination-dependent surface defect variation and antibacterial activity of magnesium oxide nanoplates, *ChemistrySelect*, **5** (2020) 3201.
18. J. P. Singh, V. Singh, A. Sharma, G. Pandey, K. H. Chae, and S. Lee, Approaches to synthesize MgO nanostructures for diverse applications, *Heliyon*, **6** (2020).
19. D. Suhag, A. Thakur, and P. Thakur, Integrated nanomaterials and their applications. Springer, (2023).
20. D. Fischer, D. Zagorac, K. Küster, and J. C. Schön, Synthesis of two structurally different MgO Films containing dioxygen species: Dioxygen embedded at grain boundaries, and as components of a superfilled rock salt structure, *Coatings*, **14** (2024) 1563.

21. Y. Li *et al*., Photocatalytic water splitting on MgO with exceptional quantum efficiencies at elevated temperatures, *Nature Communications*, **10** (2019) 4421.

22. N. H. Khdary, A. S. Alayyar, L. M. Alsarhan, S. Alshihri, and M. Mokhtar, Metal oxides as catalyst/supporter for carbon dioxide capture and conversion, review, *Catalysts*, **12** (2022) 300.

23. N.-Y. T. Nguyen, N. Grelling, C. L. Wetteland, R. Rosario, and H. Liu, Antimicrobial activities and mechanisms of MgO nanoparticles against pathogenic bacteria, yeasts, and biofilms, *Scientific Reports*, **8** (2018) 16260.

24. A. Almontasser and A. Parveen, Probing the effect of nickel, cobalt, and iron doping concentrations on the antibacterial behaviors of MgO nanoparticles, *Scientific Reports*, **12** (2022) 7922.

25. M. Chebbi, S. Mansouri, S. Hcini, I. Ghiloufi, A. Mimouni, and L. El Mir, Investigating the impact of calcination temperature on the structural and optical properties of chromium-substituted Mg-Co ferrite nanoparticles, *Journal of Molecular Structure*, **1295** (2024) 136740.

26. W. Zarai *et al*., *Journal of Inorganic and Organometallic Polymers and Materials*, **36** (2025) 243.

27. M. Chebbi, S. Mansouri, S. Hcini, N. Hamdaoui, and L. El Mir, Study of sintering temperature effects on the structural and electrical properties of mg0. 6co0. 4fecro4 ferrites synthesized by the sol-gel method, *Journal of Inorganic and Organometallic Polymers and Materials*, **33** (2023) 1201.

28. W. Jdey, T. Mzoughi, N. Hamdaoui, S. Hcini, and S. Mansouri, Impact of the calcination temperature on structural, electrical and dielectric properties for spinel ferrites, *Journal of Inorganic and Organometallic Polymers and Materials*, **33** (2023) 3485.

29. T. V. Sagar, T. S. Rao, and K. C. B. Naidu, Effect of calcination temperature on structural, magnetic, and dielectric properties of mg0.75zn0.25al0.2fe1.8o4 ferrites, *Journal of Materials Science: Materials in Electronics*, (2024).

30. R. B. Rotti *et al*., Green synthesis of MgO nanoparticles and its antibacterial properties, *Frontiers in Chemistry*, **11** (2023) 1143614.

31. S. Yousefi, B. Ghasemi, and M. P. Nikolova, Morpho/optostructural characterizations and XRD-assisted estimation of crystallite size and strain in MgO nanoparticles by applying Williamson-Hall and size-strain techniques, *Journal of Cluster Science*, **33** (2022) 2197.

32. B. Himabindu, N. L. Devi, and B. R. Kanth, Microstructural parameters from x-ray peak profile analysis by Williamson- Hall models; a review, *Materials Today: Proceedings*, **47** (2021) 4891.

33. N. Rani, S. Chahal, A. S. Chauhan, P. Kumar, R. Shukla, and S. Singh, X-ray analysis of MgO nanoparticles by modified Scherer's Williamson-Hall and size-strain method, *Materials Today: Proceedings*, **12** (2019) 543.

34. R. Balakrishnan *et al.*, Thermal decomposition behavior and characterization of magnesium oxide nanoparticles synthesized by precipitation method, *Ceramics International*, **45** (2019) 18866.

35. G. Kasi *et al*., Effect of calcination temperatures on crystallite size, particle size, and antimicrobial activity of synthesized MgO and its cytotoxicity, *International Journal of Molecular Sciences*, **26** (2025) 4868.

36. X. Zhang, Y. Zheng, X. Feng, X. Han, Z. Bai, and Z. Zhang, Calcination temperature-dependent surface structure and physicochemical properties of magnesium oxide, *RSC advances*, **5** (2015) 86102.

37. D. Harrabi, S. Hcini, J. Dhahri, N. Hamdaoui, R. Charguia, M. Bouazizi, and S. Mansouri, Structural, magnetic, and dielectric properties for Mg0 spinel ferrites prepared under different calcination temperatures, *Journal of Superconductivity and Novel Magnetism*, **36** (2023) 1549.

38. W. Jdey, N. Hamdaoui, S. Hcini, S. Mansouri, and L. El Mir, Enhancement of the optical properties of Mgo. 6 Cuo. 4 FeCrO4 spinel ferrite via heat treatment, *Optical Materials*, **147** (2024) 114666.

39. M. Bura, G. Singh, D. Gupta, N. Malik, A. Salim, A. Kumar, R. Singhal, S. Kumar, and S. Aggarwal, Transition in the preferred orientation of RF sputtered ZnO/Si thin films by thermal annealing: Structural, morphological, and optical characteristics, *Optical Materials*, **133** (2022) 113024.

40. H. T. Sim, M. Gençaslan, and M. Merdan, Synthesis of MgO nanoparticles via the sol-gel method for antibacterial applications, investigation of optical properties and comparison with commercial magnisum oxide, *Discover Applied Sciences*, **6** (2024) 577.

41. J. P. Singh and K. H. Chae, Local electronic structure perspectives of nanoparticle growth: the case of MgO, *ACS Omega*, **4** (2019) 7140.

42. S. Dolabella, A. Borzì, A. Dommann, and A. Neels, Lattice strain and defects analysis in nanostructured semiconductor materials and devices by high-resolution X-ray diffraction: Theoretical and practical aspects, *Small Methods*, **6** (2022) 2100932 .

43. H. Zhang, J. Hu, J. Xie, S. Wang, and Y. Cao, A solid-state chemical method for synthesizing MgO nanoparticles with superior adsorption properties, *RSC Advances*, **9** (2019) 2011.

44. K. Ishimoto, T. Tanaka, Y. Ohki, Y. Sekiguchi, and Y. Murata, Thermally stimulated current in low-density polyethylene/mgo nanocomposite-on the mechanism of its superior dielectric properties, *IEEJ Transactions on Fundamentals and Materials*, **129** (2009) 97.

45. T. Kikuma, N. Fuse, T. Tanaka, Y. Murata, and Y. Ohki, Filler-content dependence of dielectric properties of lowdensity polyethylene/mgo nanocomposites, *IEEJ Transactions on Fundamentals and Materials*, **126** (2006) 1072.

46. S. Mehanathan *et al*., Magnesium oxide nanoparticles for the adsorption of pentavalent arsenic from water: Effects of calcination, *Membranes*, **13** (2023) 475.

47. C. Shi *et al*., Barium titanate nanoparticles: Short-range lattice distortions with long-range cubic order, *Physical Review B*, **98** (2018) 085421.

48. T. H. Ulucan, J. Wang, E. Onur, S. Chen, M. Behrens, and C. Weidenthaler, Unveiling the structure-property relationship of MgO-supported Ni ammonia decomposition catalysts from bulk to atomic structure by in situ/operando studies, *ACS Catalysis*, **14** (2024) 2828.

49. M.-A. Gatou, N. Bovali, N. Lagopati, and E. A. Pavlatou, MgO nanoparticles as a promising photocatalyst towards rhodamine B and rhodamine 6G degradation, *Molecules*, **29** (2024) 4299.

50. J. B. Nelson and D. P. Riley, An experimental investigation of extrapolation methods in the derivation of accurate unit-cell dimensions of crystals, *Proceedings of the Physical Society*, **57** (1945) 160.

51. P. Scardi *et al.*, Size-strain separation in diffraction line profile analysis, *Journal of Applied Crystallography*, **51** (2018) 831.

52. P. P. Rodenbough, C. Zheng, Y. Liu, C. Hui, Y. Xia, Z. Ran, Y. Hu, and S.-W. Chan, Lattice expansion in metal oxide nanoparticles: MgO, Co3O4, & Fe3O4, *Journal of the American Ceramic Society*, **100** (2017) 384.

53. B. Pathak, A. Yadav, P. Choudhary, M. Varshney, and A. Mishra, Structural and phonon modes study of nano ceramics coal2o4 synthesized by sol-gel route, *in AIP Conference Proceedings*, **2100** (2019) 020175.

54. V. Daniele, A. R. Volpe, P. Cesare, and G. Taglieri, MgO nanoparticles obtained from an innovative and sustainable route and their applications in cancer therapy, *Nanomaterials*, **13** (2023) 2975.

55. Savita, M. Jain, Manju, A. Vij, and A. Thakur, Impact of annealing on the structural properties of MgO nanoparticles by XRD analysis and Rietveld refinement, *in AIP Conference Proceedings*, **2093** (2019) 020024.

56. S. Abinaya and H. P. Kavitha, MgO nanoparticles: effective antilarvicidal and antibacterial agents, *ACS Omega*, **8** (2023) 5225.

57. L. Huang, Z. Yang, and S.Wang, Influence of calcination temperature on the structure and hydration of MgO, *Construction and Building Materials*, **262** (2020) 120776.

58. J. Karamdel et al., Structural, optical and mechanical properties of mgo nanoparticles: effect of calcination temperature, *Journal of Alloys and Compounds*, **735** (2018) 123.

59. J. Madhavi, Comparison of average crystallite size by X-ray peak broadening and Williamson-Hall and size-strain plots for VO2+ doped ZnS/CdS composite nanopowder, *SN Applied Sciences*, **1** (2019) 1509.

60. J. Hornak, Synthesis, properties, and selected technical applications of magnesium oxide nanoparticles: a review, International *Journal of Molecular Sciences*, **22** (2021) 12752.

61. D. Balzar *et al.*, Size-strain line-broadening analysis of the ceria roundrobin sample, *Journal of Applied Crystallography*, **37** (2004) 911.

62. S. Alias, A. Ismail, and A. Mohamad, Effect of pH on ZnO nanoparticle properties synthesized by sol-gel centrifugation, *Journal of Alloys and Compounds*, **499** (2010) 231.

63. G. Williamson and R. Smallman, Dislocation densities in some annealed and cold-worked metals from measurements on the X-ray debye-scherrer spectrum, *Philosophical magazine*, **1** (1956) 34.